Corrosion Science 240 (2024) 112451

Contents lists available at ScienceDirect

Corrosion Science

journal homepage: www.elsevier.com/locate/corsci

Surface treatments on 3D printed Ti6Al4V biomedical plates to enhance corrosion resistance in simulated physiological solutions and under inflammatory conditions

D. Pupillo [a], F. Di Franco [b,*], D. Palmeri [b], G. Pollara [b], G. Buffa [b], L. Fratini [b], M. Santamaria [b]

[a] Dipartimento di Scienza Applicata e Tecnologia, Politecnico di Torino, Corso Duca degli Abruzzi 24, Torino 10129, Italy
[b] Dipartimento di Ingegneria, Università di Palermo, Viale delle Scienze, Palermo 90128, Italy

ARTICLE INFO

Keywords:
Additive manufacturing
Ti6Al4V
Corrosion
Biomedical plates
Inflammatory conditions
Anodic oxide

ABSTRACT

Ti6Al4V biomedical plates were fabricated by Laser Powder Bed Fusion using different process parameters. A slight influence of the laser energy density on mechanical properties and microstructure was revealed. Chemical etching allowed to make the surface of 3D samples uniform removing also spheres of unfused material. After etching some samples were anodized in calcium acetate and β-glycerolphosphate containing solution to grow a Ca and P containing porous TiO_2 layers. The chemical etching improved the corrosion resistance of the alloy in simulated body fluid, while only after anodizing the alloys resulted to be corrosion resistant under inflammatory and severe inflammatory conditions.

1. Introduction

Biomedical materials are widely studied as valuable candidates for the fabrication of implants that should replace damaged hard and soft tissues in human body. Those materials used as implants for load-bearing applications must comply several features to be durable and reliable, such as high corrosion resistance and mechanical strength, biocompatibility and good osteointegration to avoid revision surgery [1,2].

Based on these characteristics, metals and metallic alloys such as Co-Cr alloys, stainless steels, Ti and Ti alloys are suitable materials to construct implants for load-bearing applications. In particular, Ti and its alloys are very promising since they have elastic moduli close to those of bones and lower density with respect to that of Co-Cr alloys and stainless steels [3,4]. Compared to commercially pure Ti, Ti alloys have better mechanical properties that make them particularly suitable for orthopaedic and traumatology implants. Moreover, they show very good corrosion resistance in biological environment even if release of alloying elements such vanadium and aluminium can become an issue since they are considered hazardous for human body [5]. The latter phenomenon can become more dangerous when the prosthesis is implanted in highly oxidizing environment as those arising under severe inflammatory conditions. Indeed, very noble species can shift the corrosion potential toward more positive value thus inducing Al and V dissolution.

Among the advantages of using Ti alloys, it is also important to mention that in the last years several studies proved the successful fabrication of customized endoprostheses made in Ti6Al4V by laser 3D printing [6,7]. In the recent years, some papers are published on the corrosion resistance of the additively manufactured Ti6Al4V alloys for biomedical purpose [8–11].

However, there is still an issue in using this technology due to the low quality of surface finishing soon after the process. Indeed, the surface of the 3D printed metals and alloys is usually covered by not melted material powder, which can easily leave the implants and spread in the host tissue. Moreover, the presence of these spherical shaped powder particles can lead to the formation of crevices that in turn enhance the localized corrosion susceptibility. Therefore, processes suitable to remove this inhomogeneity must be designed able to clean the implants surface without affecting their corrosion resistance. In this work we studied the effect of chemical etching and of anodizing on Ti6Al4V implants prepared by Laser Powder Bed Fusion printing. A study of specimens with complex geometry that reproduces the shape of biomedical plates (3D) was carried out to investigate the effect of the geometry on their corrosion behaviour in biological environment. The surface of the devices was studied by scanning electron microscopy after chemical etching and after anodizing. Electrochemical tests were carried

* Corresponding author.
E-mail address: francesco.difranco@unipa.it (F. Di Franco).

https://doi.org/10.1016/j.corsci.2024.112451
Received 21 June 2024; Received in revised form 29 July 2024; Accepted 12 September 2024
Available online 17 September 2024

out to assess the corrosion resistance of the alloy in simulated body fluids without and with the addition of chemical species simulating inflammatory conditions as well as severe inflammatory conditions [12–17].

2. Experimental

2.1. Samples preparation

The experiments were performed on an SLM 280HL machine using Ti6Al4V ELI-grade powder from SLM Solutions Group AG (Lübeck, Germany) with a mass density of 4.43 g/cm^3 and a 20–63 μm size distribution. All the samples were made by preheating a CP-Ti solid substrate at 200°C. Argon was used to decrease the oxygen level to 0.1 % by filling the build chamber. An overview of the nine process parameter combinations that are used in the process is provided in Table S1. The 3D geometries (Fig. 1) that have been examined replicate the features of biomedical plates usually used for humerus fracture fixation.

The printing process was done in a 90-degree building orientation, with the longitudinal axis of the plates orthogonal to the printing plate. By making this choice, it was possible to limit the extent of surfaces that were affected by the presence of supports. Three Line Energy Density (LED) values 0.11 J/mm, 0.25 J/mm, and 0.41 J/mm as well as three distinct scan algorithms were examined. The scanning strategies that were employed are as follows: a 0° starting angle, a 180° limiting scanning window, and increasing scanning angles of 15°, 45°, and 90° between successive layers. The sample are identified by using the LED values and scanning strategies (i.e. 0.11 / 15°, 0.11 / 45°, 0.11 / 90°, 0.25 / 15°, 0.25 / 45°, 0.25 / 90°, 0.41 / 15°, 0.41 / 45°, 0.41 / 90°). In Table S1, process parameters used are reported. Vacuum stress relief treatment was not carried out on the samples as the reduced cross-section geometry and 90° printing direction are conditions that reduce significantly the presence of residual stress. Three samples were produced for each set of process parameters. Microstructural examination of sample longitudinal sections, density measurements, and corrosion resistance testing were conducted using three distinct repetitions of 3D specimens. To conduct tensile tests, additional specimens shaped like dog bones were made.

To evaluate the effectiveness of the process parameters, density measurements on 3D samples were performed using the Archimedes method at room temperature following ASTM B96208. Each specimen mass in both air and fluid was measured using a Mettler Toledo balance with a precision of 0.1 mg. The relative density of the printed parts was estimated using the Ti6Al4V density, which is 4,43 g/cm^3. The dog bone-shaped samples with a rectangular cross-section (15 × 2 mm) and a suitable gauge length of 30 mm were made as a reduction of Standard ASTM/E8 to assess the mechanical performance in terms of ultimate tensile strength and ductility (elongation to failure). The Galdabini universal testing machine was utilized to carry out the tensile tests. The microstructural modifications that occur as a result of the used process parameters were evaluated by etching the specimens with Kroll's reagent and observing them through an Olympus Optical microscope after grinding and polishing. The metallographic observations were conducted by preparing a longitudinal section of the samples. The as printed samples (AP) were characterised without successive treatment to understand if there is an effect of the different process parameter used on the corrosion resistance. Subsequently, 3D samples were chemical etched (CE) in a solution of 1:4:5 vol ratio of HF (40 %): HNO_3 (68 %): H_2O in an ultrasonic bath for 5 minutes. The etching process was optimized to remove the unfused powder from the surface. Finally, the samples were anodized in aqueous solution to growth a thick porous layer to improve corrosion resistance and osteointegration. The anodizing process was carried out galvanostatically at 20 mA cm^{-2} and a voltage compliance of 200 V in an aqueous solution containing 0.2 M calcium acetate ($(CH_3COO)_2Ca{\cdot}H_2O$) and 0.04 M β-glycerol phosphate disodium pentahydrate (β-GPDS, $C_3H_7Na_2O_6P{\cdot}5\ H_2O$). A two-electrode configuration was used where the alloy was the anode (working electrode) and Al 99.9 % foil was the cathode (counter electrode).

2.2. Sample characterization

The samples (as printed, chemical etched and anodized) were examined by scanning electron microscopy (SEM) using a FEI Quanta 200 FEG SEM instrument at several magnifications, combined with a X-ray energy dispersive system (EDX).

The crystalline structure of as printed samples was investigated using. a PANalytical Empyrean diffractometer equipped with a PIXcel1D (tm) detector using the Cu$K\alpha$ radiation. In order to achieve the highest signal-to-noise ratio, the operating conditions were 40 V and 40 mA.

Raman analysis was performed through a Renishaw inVia Raman Microscope spectrometer equipped with a microprobe (50×) and a CCD detector with a Nd:YAG laser with a wavelength of 532 nm. Contact angle was measured using FTA 1000 instrument, with 5 μL droplets of deionized water. Measurements were repeated at least three times in several spots of the samples.

For metal ions release tests, PerkinElmer Inc.-Optima 2100 DV was used for ICP–OES analysis. To estimate metal release in solution, a calibration procedure was carried out with 0 (ultrapure water), 2, 5, 10,

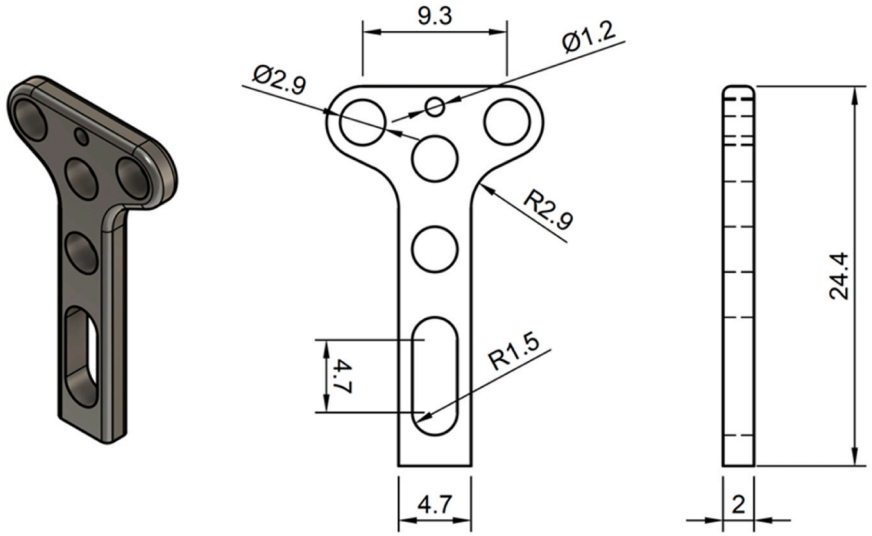

Fig. 1. 3D CAD model and quoted sketch of the printed biomedical plates.

20, 50, 100, 200, and 500 ppb for Ti, Al, and V standard solutions.

The experimental setup used for the photoelectrochemical investigations consists of a 450 W UV–VIS xenon lamp coupled with a monochromator (Kratos), which allows monochromatic irradiation of the specimen surface through the photoelectrochemical cell quartz windows. A two-phase lock-in amplifier (EG&G) was used in connection with a mechanical chopper (frequency: 13 Hz) to separate the photocurrent from the total current circulating in the cell due to the potentiostatic control. Photocurrent spectra are corrected for the relative photon flux of the light source at each wavelength; the photocurrent yield in arbitrary current units is represented in the y axis.

The corrosion resistance was evaluated in three simulating solutions i.e. Hanks' balance salt solutions (HBSS), inflammatory conditions (HBSS_IC) and severe inflammatory conditions (HBSS_SIC), see composition at Table 1, at 37°with a Parstat 2263. Electrochemical characterizations were carried out using a standard three electrode configuration with a platinum mesh as counter electrodes and an Ag/AgCl as a reference electrode (3.5 M KCl, 0.2 V vs. SHE). The open circuit potential (OCP) was recorded for 1 hour and EIS spectra were generated at OCP by applying a sinusoidal signal of amplitude 10 mV over the frequency range 0.1 Hz - 100 kHz. The resultant spectra were analyzed with Zview software. Polarization curves were recorded starting from −200 mV vs. OCP to +2 V vs. Ag/AgCl with a scan rate of 5 mVs^{-1}.

3. Results and discussions

3.1. Mechanical and microstructural characterizations

Fig. 2 displays the results of the mechanical characterization and the density measurements of the samples as a function of the printing conditions. The mechanical characterization of the samples, in terms of Ultimate Tensile Strength (UTS) and Elongation to Failure (ETF) values reported in Fig. 2a, highlighted that low (0.11 J/mm) and high (0.41 J/mm) LED values determine a decrease in the mechanical resistance of the material and of its ductility compared to the values obtained for LED equal to 0.25 J/mm. According to Fig. 2b, the highest density values are measured for LED 0.25 J/mm, while for lower or higher LED values the density of the material tends to decrease.

The results of the microstructural analysis, shown in Fig. 3, highlighted the presence of porosity due to a lack of fusion and gas porosity in the samples made with 0.11 J/mm and 0.41 J/mm LEDs, respectively. These defects justify the trends previously discussed about the resistance and density characteristics of the samples as the process parameters vary. Defects of high porosity due to gas or lack of fusion produce a reduction in the strength and ductility characteristics of the material. The porosity detected is uniformly distributed near the external surface of the samples, as shown in Fig. 3, the porosity detected is not connected with continuity. The microstructure observed for all the samples is of the lamellar type α' which is formed following the rapid cooling associated with the process. The α' lamellar structure forms within the stable β grains at high temperatures. The average size of the original β grain, within which the structure α' develops, depends on the value of LED. As the value of LED increases, the average size of the original grain β increases. In the case shown in Fig. 3, corresponding to the scan strategy value of 45°, the average original grain size β takes on average values of 80 μm, 110 μm and 150 μm, respectively, when the LED values are 0.11 J/mm, 0.25 J/mm and 0.41 J/mm.

Table 1
Composition of simulating solutions employed.

Component	HBSS	HBSS_IC	HBSS_SIC
NaCl	8 g l^{-1}	8 g l^{-1}	8 g l^{-1}
KCl	0.4 g l^{-1}	0.4 g l^{-1}	0.4 g l^{-1}
$NaHCO_3$	0.35 g l^{-1}	0.35 g l^{-1}	0.35 g l^{-1}
$NaH_2PO_4{\cdot}H_2O$	0.25 g l^{-1}	0.25 g l^{-1}	0.25 g l^{-1}
$Na_2HPO_4{\cdot}H_2O$	0.06 g l^{-1}	0.06 g l^{-1}	0.06 g l^{-1}
$CaCl_2{\cdot}2\ H_2O$	0.19 g l^{-1}	0.19 g l^{-1}	0.19 g l^{-1}
$MgCl_2$	0.19 g l^{-1}	0.19 g l^{-1}	0.19 g l^{-1}
$MgSO_4{\cdot}7\ H_2O$	0.06 g l^{-1}	0.06 g l^{-1}	0.06 g l^{-1}
Glucose	1 g l^{-1}	1 g l^{-1}	1 g l^{-1}
H_2O_2	-	150 mM	150 mM
FBS	-	-	10 % wt
Lactic Acid	-	-	150 mM
pH	7.2	5.2	2.2

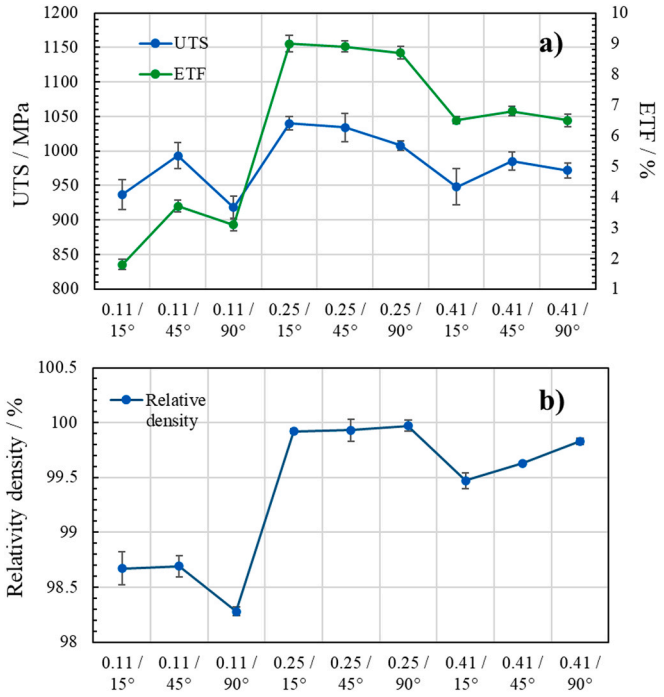

Fig. 2. a) Mechanical characteristics (UTS and ETF) and b) density for each process parameters.

In Fig. 4 and S1, XRD patterns reveal the presence of dominated by α'/α -Ti phase for the different LED values used. A weak reflection at $2\theta = 39.7°$, relating to β-Ti phase, is present for 3D samples produced with 0.41 J/mm as LED value. This condition is due to an intensification of the material heat treatments for high LED associated with low layer thickness values. As reported in literature, the formation of phase α + β is enabled starting from phase α' which is formed in the first instance. Varying the scanning strategy for fixed LED value, homogeneous trends of the XRD pattern are observed [18,19].

3.2. Morphological characterizations

Fig. 5 shows the SEM micrographs of the surface of as printed, chemically etched and chemically etched anodized 3D printed Ti alloys. It is evident that unfused powder is still present on the surface of the as printed samples, typical of 3D printed materials produced by LPBF (see Fig. 5a). This inhomogeneity results also in a not uniform wettability of the surface, evidenced by contact angle measurements revealing a large variability all over the surface (see Figure S2). These particles are likely to be detached by the alloys in aqueous solution especially in presence of flowing solution and/or wear, thus a preliminary surface treatment that leaves a smoother surface with good corrosion resistance must be carried out to remove them before device implantation. For these reasons, a chemical etching in hydrofluoric acid and nitric acid containing ultrasonicated aqueous solution for 5 minutes was carried out. This chemical etching allows the complete removal of the powder with consequent improvement of the homogeneity of the samples surface as evident in the SEM micrograph of Fig. 5b. Measured water contact angle (reported in figure S3) reveal a low variability in term of wettability for samples

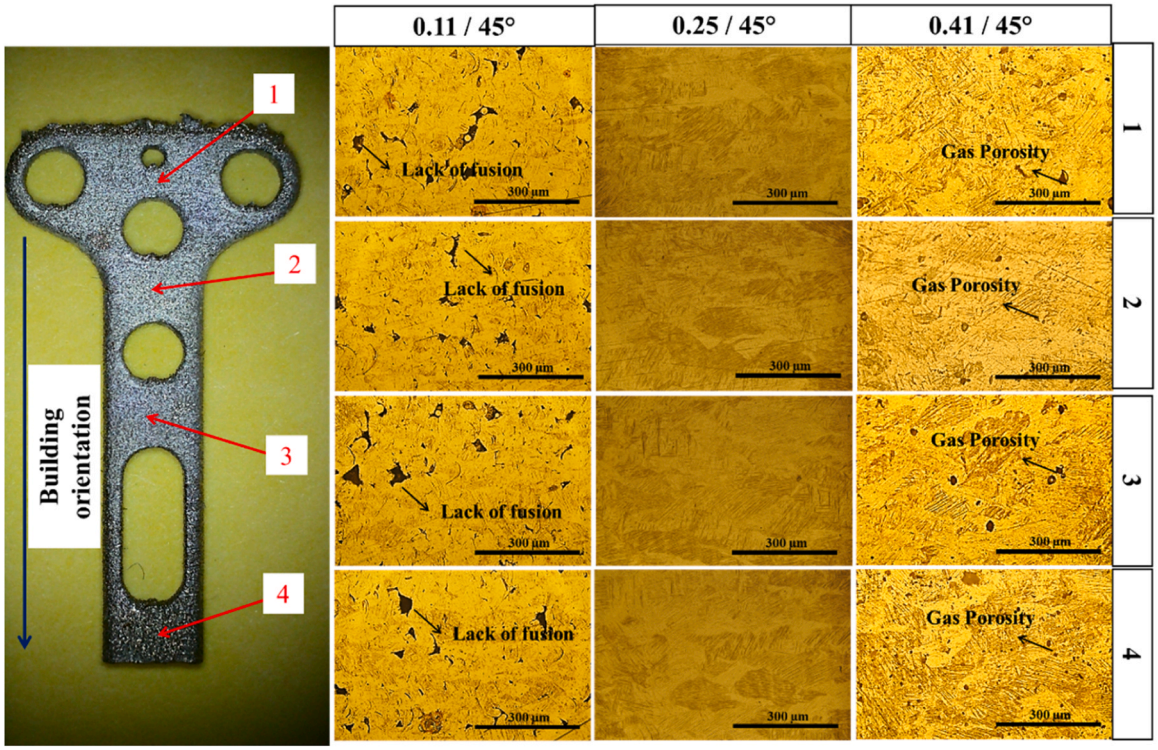

Fig. 3. Micrographs for as-built 3D Ti6Al4V sample longitudinal sections were taken using an optical microscope for 0.11 J/mm, 0.25 J/mm, and 0.41 J/mm LED and a 45° scan strategy.

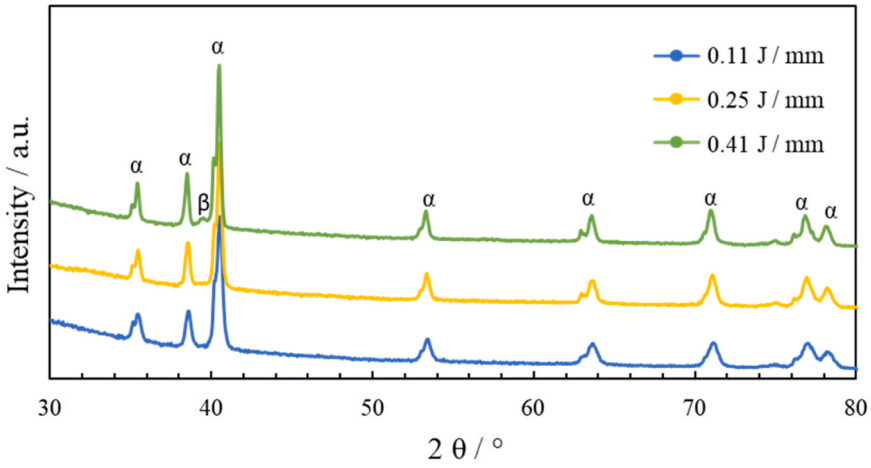

Fig. 4. XRD pattern for as printed 3D Ti6Al4V sample for different LED values, as 0.11 J/mm, 0.25 J/mm, 0.41 J/mm with 90° as scanning strategy.

after the chemical etching if compared to as printed samples. Chemically etched samples were then anodized to 200 V as described in the experimental section. Despite the different microstructure revealed by optical microscopy of the printed samples with respect to cast alloy, the voltage time transient under galvanostatic regime is similar to that recorded with cast alloys (see Figure S4) with consequent development of a porous oxide layer on the alloy surface, as disclosed by the SEM images of Fig. 5c-d. The treatment allows to measure almost the same contact angle all over the surface (57° ± 10°, see Figure S5), indicating the formation of a hydrophilic layer. According to Raman Spectroscopy, the anodic film is mainly constituted by anatase as suggested by the Raman bands at E_g (144, 196, and 638 cm^{-1}), $B_{1\,g}$ (398 and 519 cm^{-1}) and $A_{1\,g}$ (513 cm^{-1}) (see Figure S6). The Raman bands are shifted if compared to crystalline anatase phase by a few cm^{-1}, suggesting the formation of a defective TiO_2 layer. It is important to mention that, as reported for cast alloys, the anodizing leads to the incorporation of calcium and phosphates ions from the electrolyte (see EDX in Fig. 5e), with consequent improvement of osteointegration properties [20–22]

A photoeletrochemical characterization was carried out to get information about the electronic properties of the anodic films on the 3D printed alloys, that strongly affect the corrosion resistance of the samples. Fig. 6 shows the photocurrent spectrum (photocurrent vs wavelength curve) recorded at 1.5 V vs. SSC in HBSS.

Assuming indirect optical transitions, it is possible to estimate the band gap values according to the following equation:

$$(Q_{ph}\ h\nu)^{0.5} \sim (h\nu - E_g) \quad (1)$$

where, for photon energy in the vicinity of band gap, Q_{ph}, the photocurrent yield, is proportional to the light absorption coefficient, $h\nu$ is the photon energy and E_g is the optical band gap.

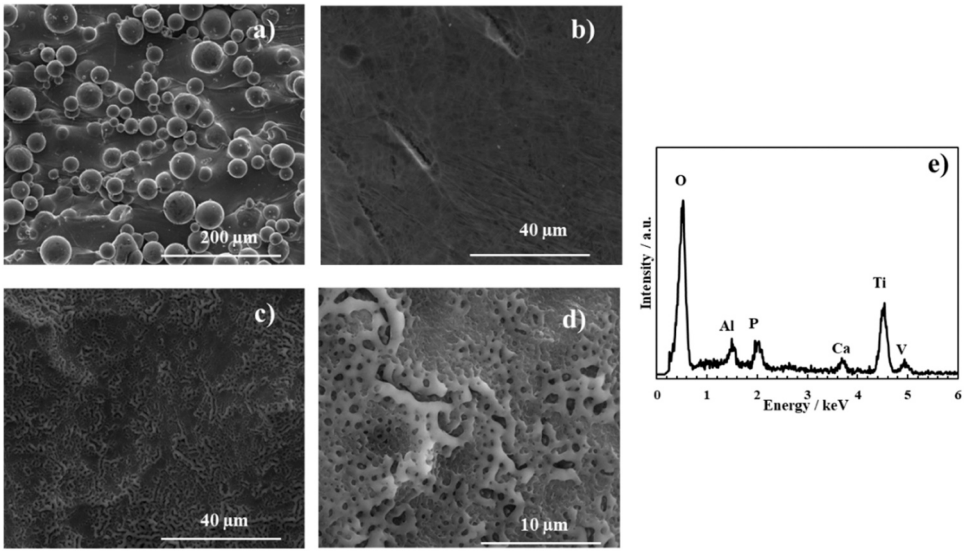

Fig. 5. SEM micrographs for a) as printed, b) chemically etched and c-d) anodized with relative e) EDX analysis related to 3D Ti6Al4V samples.

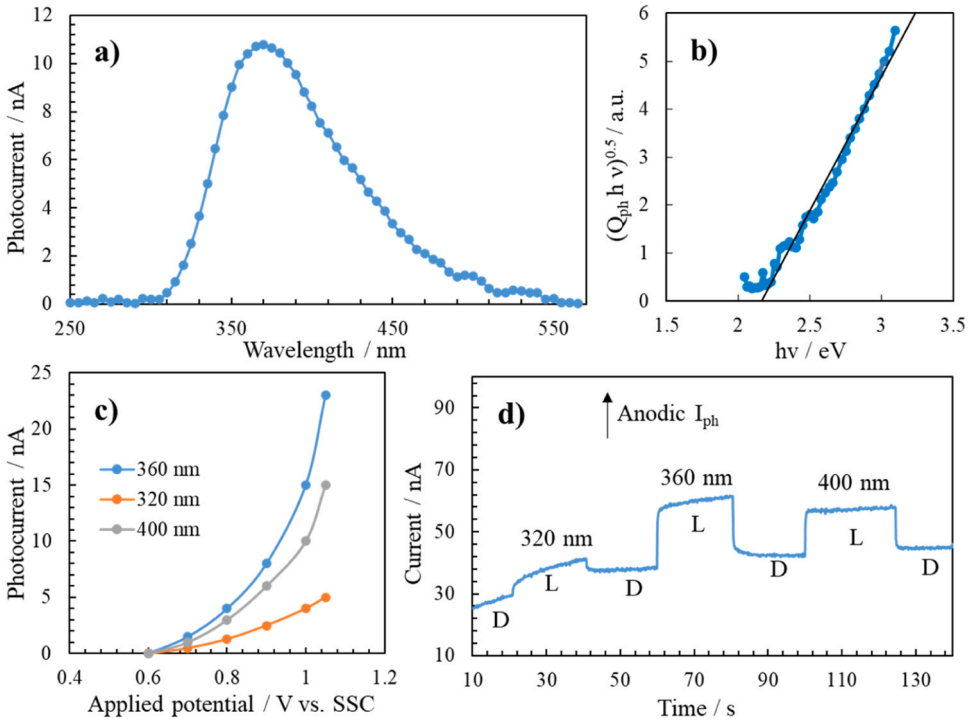

Fig. 6. Photoelectrochemical characterization in HBSS of anodized 3D Ti6Al4V samples a) Photocurrent spectrum recorded at 1.5 V vs. SSC b) $(Q_{ph}\ hv)^{0.5}$ vs. hv relating to Fig. 6a, c) photocharacteristics recorded at different wavelengths and d) current vs. time curves recorded by manually chopping the irradiation at different wavelengths. L: light, D: dark.

A band gap of 2.15 eV can be estimated for the anodic layer, which is significantly lower than that reported in the literature for anodic TiO_2 (3.3 eV) in agreement with previous experimental findings on anodic films grown on cast Ti6Al4V. The anodic film is a n-type semiconductor, as confirmed by recording photocurrent transients under constant irradiating wavelengths (see Fig. 6d) and by the photocharacteristics, i.e. photocurrent vs potential curves (see Fig. 6c). Notably, for the oxide grown on 3D samples, stationary anodic photocurrent was measured (see Fig. 6d) and the photocurrent decreases by shifting the potential toward the negative direction as expected for n-type SC, and the zero-photocurrent potential can be assumed as an estimate of the flat band potential of the oxide.

3.3. Corrosion behaviour in simulated body fluid

The corrosion resistance of 3D printed samples without and with successive surface treatments in different simulating body environments was studied by electrochemical tests, namely by recording electrochemical impedance spectra and polarization curves. In Fig. 7a,b, impedance spectra (EIS) in the Bode representation related to as printed 3D samples with LED = 0.25 J/mm recorded in HBSS at 37°C and at the corresponding open circuit potential are reported. EIS spectra and polarization curves for the other 3D samples (with LED = 0.11 and 0.41 J/mm) are reported in figure S7.

In the case of as printed 3D samples, the EIS spectra can be simulated

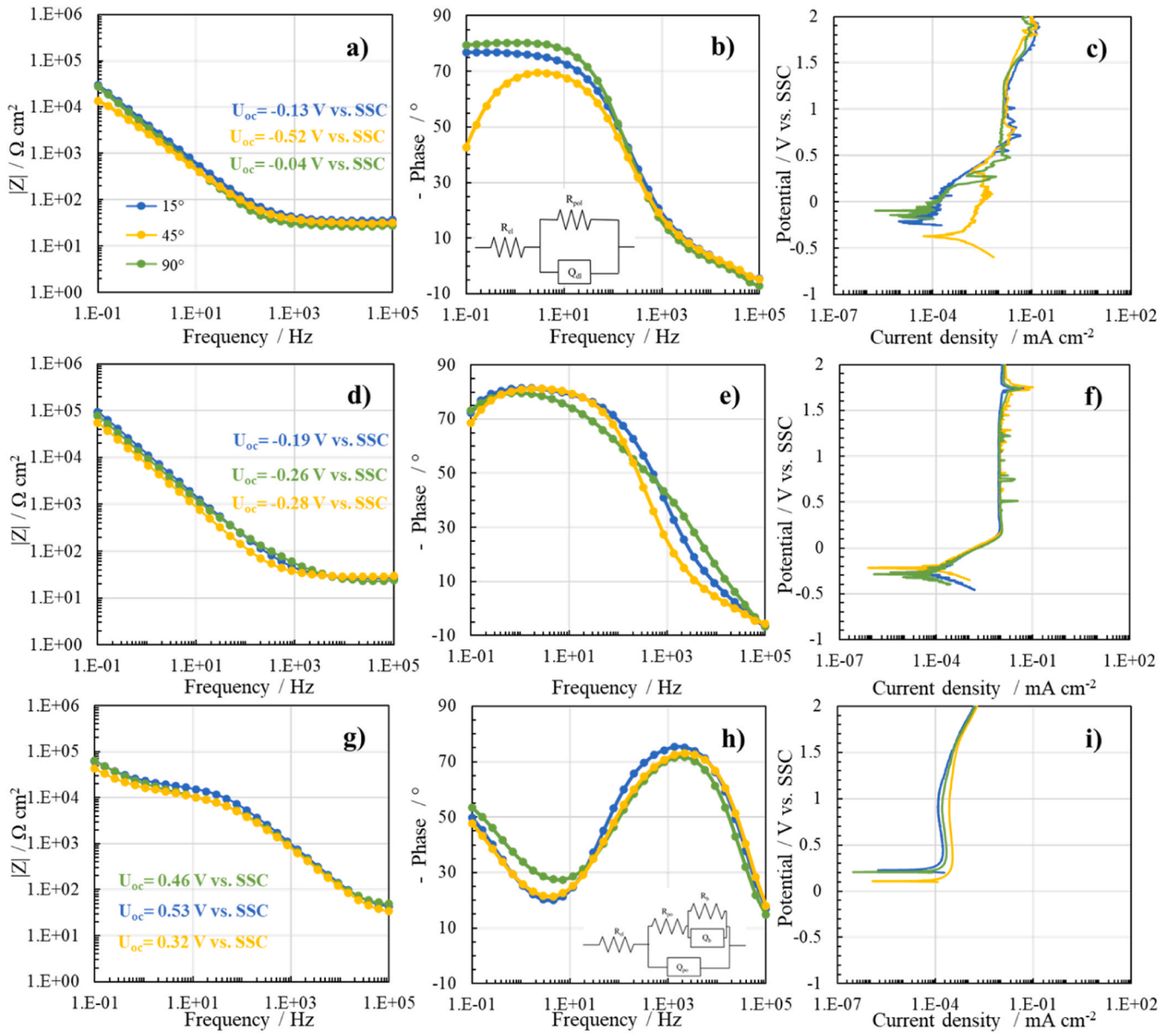

Fig. 7. EIS spectra in Bode representation (at corresponding open circuit potential U_{oc}) and polarization curves recorded in HBSS related to a, b, c) as printed, d, e, f) chemically etched and g, h, i) anodized 3D samples with 0.25 J/mm as LED value and relative electric equivalent circuits.

using a simple one-time constant EEC, see Fig. 7b, where R_{el} is the electrolyte resistance in series with a parallel between polarization resistance, R_{pol}, and Q_{dl}, i.e. a constant phase element accounting for the not ideal double layer capacitance of the alloy. To estimate the effective double layer capacitance from the CPE value, we used the following relationship [23]:

$$C_{dl} = Q_{dl}^{1/n} R_{el}^{(1-n)/n} \quad (2)$$

The contribution to the measured capacitance arising from the thin TiO_2 passive layer grown by air exposure on the surface of the alloys is negligible, since due to the negative open circuit potential, the layer is very close to or below its flat band potential, thus being under forward bias regime [24,25]. The corresponding fitting parameters are presented in Table 2 and table S2. The polarization resistance is very high, but in the case of plates printed with a scanning strategy of 45° a lower R_{pol} is measured (by at least one order of magnitude). For these alloys a very negative open circuit potential is measured, suggesting a not perfect passivation of the samples (see Fig. 7a). These results agree with the polarization curves reported in Fig. 7c and S7 showing a higher corrosion current density for alloys printed with 45° scanning strategy. Moreover, all the as printed samples show a passivation range between 0.5 and 1.5 V vs. SSC and an anodic peak due to vanadous ions release. Notably, current oscillations are clearly visible, suggesting the formation of metastable pits and/or to the detachment of debris on the surface. Ti alloys are not susceptible to pitting at this low chloride ions concentration, therefore the occurrence of this phenomenon can be attributed to the alloy surface roughness left by the 3D printing.

Table 2
Fitting parameters related to the impedance spectra shown in Fig. 7a,b recorded for as printed 3D samples with 0.25 as LED value.

Process parameter	R_{el} /Ω cm²	R_{pol} /Ω cm²	C_{dl} /F cm^{-2}	χ^2
0.25/15°	36	4.00E+06	1.48E−05	2.00E−03
0.25/45°	32	2.80E+04	1.80E−05	1.47E−03
0.25/90°	27	2.24E+06	2.39E−05	2.00E−03

Fig. 7d,e and S8 show EIS spectra in the Bode representation for chemically etched alloys, recorded in HBSS at 37°C and the relative open circuit potential U_{oc}. After the chemical etching a slight increase of the overall impedance is observed if compared to as printed samples. The fitting parameters according to the EEC of Fig. 7a, are reported in Table 3 and Table S3. The polarization curves recorded in HBSS at 37°C display a passivation range between +0.2 and 2 V vs. SSC wider than that of the as printed samples, with a less pronounced anodic peak due to vanadous ions dissolution. The results obtained in terms of overall impedance and i_{corr} show that the corrosion resistance obtained for 3D samples are comparable to the results obtained for cast Ti alloy [14,15,26]. However, current oscillations are clearly visible in the polarization curves also for etched samples.

Fig. 7g,h shows EIS spectra in Bode representation related to anodized 3D printed with LED = 0.25 J/mm. The EIS spectra for LED = 0.11 and 0.41 J/mm are reported in figure S9. For anodized alloys, the EEC consists of a Q_{po}, a CPE modelling the pore wall non ideal capacitance, in parallel with a series between R_{po}, the electrolyte resistance inside the pore, and the (R_b Q_b) parallel, related to the barrier oxide layer presence at the bottom of the pore, see Fig. 7h. The corresponding fitting parameters, reported in Table 4 and TableS4, clearly show an increase of the overall impedance of the sample due to the presence of the porous anodic layer. Notably, the contribution attributed to the barrier film is comparable to that measured with as built and not anodized alloys. The open circuit potential in HBSS (~ 0.4 V vs Ag/AgCl) is lower than the flat band potential, thus the barrier film is under forward bias regime with an impedance comparable to that of not anodized alloys. However, the presence of a thick porous layer introduces a further contribution to the impedance, which raises significantly.

Fig. 7i shows the polarization curves related to 3D sample after the anodizing process. The presence of the anodic oxide shifts the corrosion potential toward more positive value, reduces the passivity current density and the corrosion current density with respect to as printed and chemically etched samples. Moreover, no current oscillations are visible in the polarization curves, suggesting that the anodic film hinders the formation of metastable pits and/or to the detachment of debris on the surface. According to the above reported results, the corrosion resistance in simulated body fluid of 3D printed anodized alloys is better than that of as built and chemically etched materials for all the printing parameters.

3.4. Corrosion behaviour in simulated inflammatory and severe inflammatory conditions

In order to understand the behaviour of Ti alloys in inflammatory and severe inflammatory conditions, we recorded impedance spectra at the open circuit potential at 37°C and then polarization curves using different physiological solutions, whose composition is reported in Table 1. The EIS spectra and polarization curves are reported in Fig. 8, while the corresponding fitting parameters are reported in Tables 5 and 6.

According to the EIS spectra and relative fitting parameters, there is a reduction of about two orders of magnitude for the polarization resistance for chemically etched samples in inflammatory and severe inflammatory conditions if compared to Hanks' balance salt solution. For the 3D sample after the anodizing process, no significant reduction of the impedance was observed. In addition, a reduction of about one order of magnitude for C_b recorded in inflammatory conditions (see Table 6), was observed if compared to anodized 3D sample in HBSS (see Table 4). The open circuit potential under inflammatory condition is more positive due to the presence of highly oxidizing species such as H_2O_2, therefore the anodic film is under reverse bias regime, thus the occurrence of electrochemical reactions on the sample surface is hindered [25]. Polarization curves in Fig. 8c shows that there is substantial shift for the E_{corr} to more positive values, a reduction in terms of i_{corr} and i_{pass} for 3D sample after anodizing process if compared to chemically etched samples.

Table 3
Fitting parameters related to the impedance spectra shown in Fig. 7d,e recorded for chemically etched 3D samples with 0.25 as LED values.

Process parameter	R_{el} / Ω·cm^2	R_{pol} / Ω·cm^2	C_{dl} /F cm^{-2}	χ^2
0.25/15°	27.4	1.20E+06	6.33E−06	4.70E−03
0.25/45°	29.6	2.80E+05	1.21E−05	2.40E−03
0.25/90°	25	6.00E+06	4.24E−06	2.35E−03

Long immersion tests were also carried out to assess the corrosion resistance under inflammatory conditions of chemically etched and anodized samples. Fig. 9 shows the EIS spectra recorded at corresponding open circuit potential in HBSS_IC at 37°C after 1 week of immersion. In both cases a one-time constant circuit (see Fig. 7b) very well fits the spectra and the corresponding fitting parameters are reported in Table 7. The magnitude of C_{dl} raised by almost one order of magnitude after 1 week of immersion that can be explained by the reduction of TiO_2 passive layer thickness. Moreover, in spite polarization resistance is still high for both surface treatments (R_{pol} ~ 10^5 Ω cm^2), the overall impedance decreased with respect to that measured before the immersion test. A careful inspection of the alloys' surface after long immersion tests using SEM suggests the occurrence of corrosion phenomena. According to the micrographs of Fig. 10, corrosion mainly takes place in some areas of the sample as selective attack of the edge of the melt pool probably assisted by the presence of chlorides ions. Conversely for the anodized samples the long immersion in SBF_IC induces a uniform dissolution of the outer porous oxide layer, thus leaving the alloy surface still protected (see Fig. 10). Ti ions release of about 35 μg cm^{-2} after 1 week of immersion in HBSS_IC, see figure S10, is still under the threshold limit granting biocompatibility of the plates [16,17,27] Al and V ions release is under the detection limits of the instruments.

4. Conclusions

Ti6Al4V plates were fabricated by 3D printing using different scanning strategies. According to the mechanical characterization and to the microstructure analysis there is no significant influence of the printing parameters of the alloy's corrosion behaviour. The mechanical characterization showed that high porosity defects due to gas (LED = 0.41 J/mm) or lack of fusion (LED = 0.11 J/mm) lead to a reduction in the strength and ductility characteristics of the material. X-ray diffraction evidenced the reflections of alpha phase for all the printing parameters with the presence of also beta phase for those built at LED = 0.41 J/mm. The surface of the as built samples shows the presence of unfused powder that can be successfully removed by a chemical etching in acidic aqueous solution. The 3D printed samples were also anodized in calcium acetate and beta glycerol-phosphate containing aqueous solution. The process allowed to the formation of a porous TiO_2 layers containing Ca and P. The latter is a n-type semiconductor with a very positive flat band potential according to its photoelectrochemical characterization. The corrosion resistance of the alloys resulted to be strongly influenced by both chemical etching and anodizing. According to the electrochemical impedance spectra and polarization curves both surface treatments allowed to enhance corrosion resistance of the alloys, with anodizing suppressing also the onset of metastable pits formation and/or to the detachment of debris on the surface. Under inflammatory conditions the anodic layer is able to hider the onset of localized corrosion and the consequent release due to selective attack of the edge of the melt pool with a strong beneficial effect under aggressive conditions as those typical of inflammatory conditions.

CRediT authorship contribution statement

Livan Fratini: Supervision, Resources. **Monica Santamaria:** Writing – review & editing, Supervision, Resources, Funding acquisition,

Table 4
Fitting parameters related to the impedance spectra shown in Fig. 7g,h recorded for 3D samples after the anodizing process.

Process parameter	R_{el} / Ω·cm^2	C_{po} / F cm^{-2}	R_{pol} / Ω·cm^2	R_b / Ω·cm^2	C_b /F cm^{-2}	χ^2
0.25/15°	37	1.10E−07	1.62E+04	5.00E+06	8.01E−07	1.40E−03
0.25/45°	28	1.20E−07	1.01E+04	3.00E+06	5.24E−07	3.10E−03
0.25/90°	43	1.20E−07	9.32E+03	3.00E+06	2.56E−07	2.90E−03

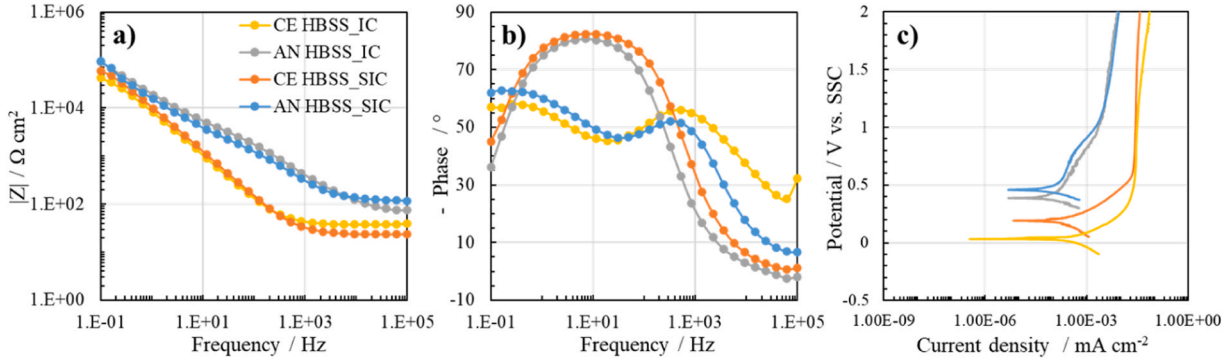

Fig. 8. EIS spectra in Bode representation and polarization curves related to chemically etched and anodized 3D samples with 0.25 J/mm as LED value in inflammatory and severe inflammatory conditions.

Table 5
Fitting parameters related to the impedance spectra shown in Fig. 8 recorded for 3D samples after the chemical etching process in inflammatory and severe inflammatory conditions.

Simulating solutions	R_{el} / Ω·cm^2	R_{pol} / Ω·cm^2	C_{dl} / F cm^{-2}	χ^2
Inflammatory conditions	37	5.7E+04	1.10E−05	5.80E−04
Severe inflammatory conditions	24	9.02E+04	1.52E−05	6.47E−04

Conceptualization. **G. Pollara:** Investigation, Data curation. **Gianluca Buffa:** Supervision. **Francesco Di Franco:** Writing – review & editing, Supervision, Data curation. **Dina Palmeri:** Investigation, Data curation. **Davide Pupillo:** Writing – original draft, Methodology, Investigation, Data curation.

Declaration of Competing Interest

The authors declare that they have no known competing financial interests or personal relationships that could have appeared to influence the work reported in this paper

Table 7
Fitting parameters related to the impedance spectra shown in Fig. 9 recorded for 3D samples after 1 week of immersion in inflammatory conditions.

Sample	R_{el} / Ω·cm^2	R_{pol} / Ω·cm^2	C_{dl} / F cm^{-2}	χ^2
Chemically etched	24	3.6E+05	9.86E−05	1.2E−02
Anodized sample	28	2.9E+05	1.80E−05	1.5E−03

Table 6
Fitting parameters related to the impedance spectra shown in Fig. 8 recorded for 3D samples after the anodizing process in inflammatory and severe inflammatory conditions.

Simulating solutions	R_{el} / Ω·cm^2	C_{po} / F cm^{-2}	R_{pol} / Ω·cm^2	R_b / Ω·cm^2	C_b /F cm^{-2}	χ^2
Inflammatory conditions	55	1.52E−07	9225	0.70E+06	4.85E−08	4.85E−08
Severe inflammatory conditions	75	4.52E−07	3182	1.20E+06	4.55E−08	4.55E−08

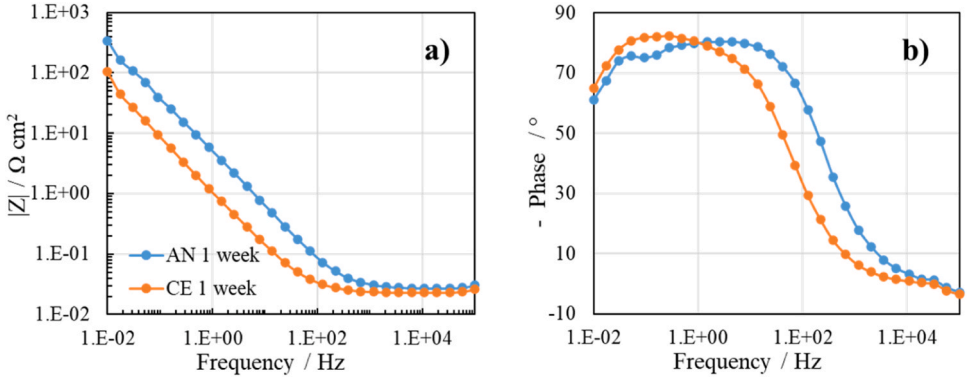

Fig. 9. EIS Spectra in Bode representation for chemically etched and anodized 3D Ti6Al4V samples after 1 week of immersion in simulated inflammatory conditions.

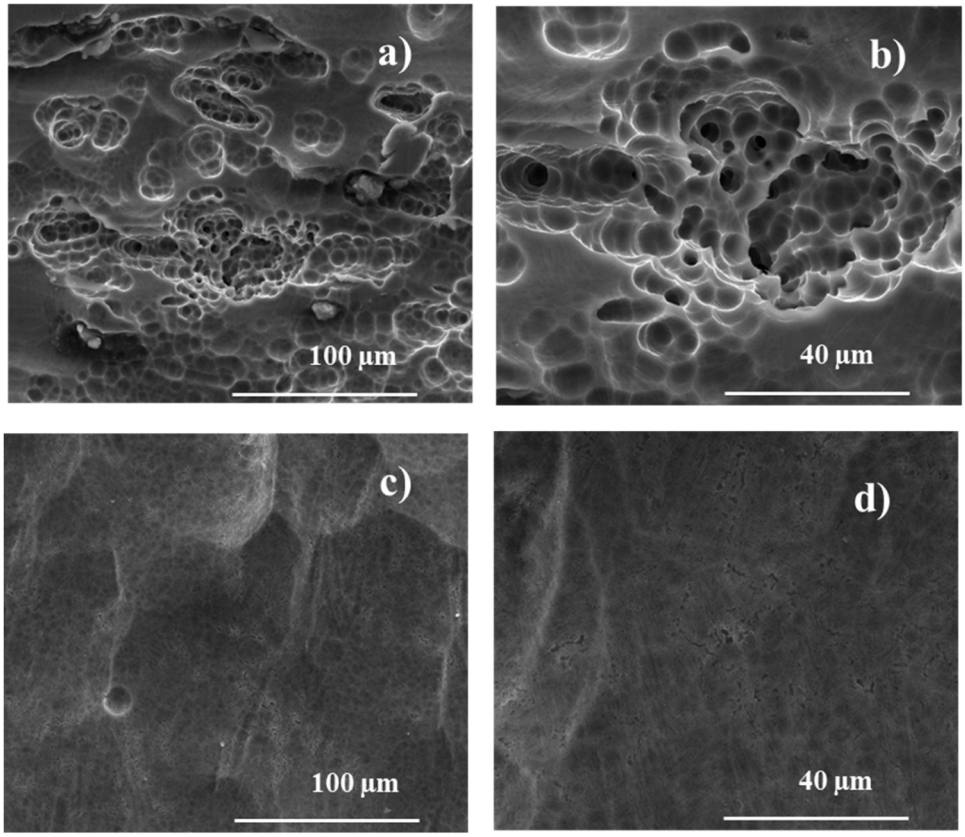

Fig. 10. SEM micrographs for a) and b) chemically etched and c) and d) anodized 3D Ti6Al4V samples after 1 week of immersion in simulated inflammatory conditions.

Data Availability

Data will be made available on request.

Acknowledgements

M.S. and F.D.F. acknowledge the European Union (NextGeneration EU), for the support through the MUR-PNRR project SAMOTHRACE.

Appendix A. Supporting information

Supplementary data associated with this article can be found in the online version at doi:10.1016/j.corsci.2024.112451.

References

[1] B. Zhang, J. Li, L. He, H. Huang, J. Weng, Bio-surface coated titanium scaffolds with cancellous bone-like biomimetic structure for enhanced bone tissue regeneration, Acta Biomater. 114 (2020) 431–448, https://doi.org/10.1016/j.actbio.2020.07.024.

[2] D. Pupillo, A. Zaffora, F. Di Franco, P. Picone, D. Nuzzo, M. Santamaria, Enhancing biocompatibility and antibacterial activity of Ti6Al4V by entrapping Ag and hydroxyapatite inside alginate filled pores of TiO2 layer grown by spark anodizing, Adv. Mater. Interfaces 10 (2023), https://doi.org/10.1002/admi.202201725.

[3] E. Estrada-Cabrera, L.R. Torres-Ferrer, O.G. Aztatzi-Aguilar, A. De Vizcaya-Ruiz, M. A. Meraz-Rios, D.G. Zarate-Triviño, A. Arizmendi-Morquecho, A. de Luna Bugallo, E. Prokhorov, G. Luna-Barcenas, Chitosan-bioglass coatings on partially nanostructured anodized Ti-6Al-4V alloy for biomedical applications, Surf. Coat. Technol. 375 (2019) 468–476, https://doi.org/10.1016/j.surfcoat.2019.07.002.

[4] A.C. Alves, F. Wenger, P. Ponthiaux, J.P. Celis, A.M. Pinto, L.A. Rocha, J.C. S. Fernandes, Corrosion mechanisms in titanium oxide-based films produced by anodic treatment, Electro Acta 234 (2017) 16–27, https://doi.org/10.1016/j.electacta.2017.03.011.

[5] M. Prestat, D. Thierry, Corrosion of titanium under simulated inflammation conditions: clinical context and in vitro investigations, Acta Biomater. 136 (2021) 72–87, https://doi.org/10.1016/j.actbio.2021.10.002.

[6] A.L. Jardini, M.A. Larosa, R.M. Filho, C.A.D.C. Zavaglia, L.F. Bernardes, C. S. Lambert, D.R. Calderoni, P. Kharmandayan, Cranial reconstruction: 3D biomodel and custom-built implant created using additive manufacturing, J. Cranio-Maxillofac. Surg. 42 (2014) 1877–1884, https://doi.org/10.1016/j.jcms.2014.07.006.

[7] A.L. Jardini, M.A. Larosa, C.A. de Carvalho Zavaglia, L.F. Bernardes, C.S. Lambert, P. Kharmandayan, D. Calderoni, R. Maciel Filho, Customised titanium implant fabricated in additive manufacturing for craniomaxillofacial surgery: this paper discusses the design and fabrication of a metallic implant for the reconstruction of a large cranial defect, Virtual Phys. Prototyp. 9 (2014) 115–125, https://doi.org/10.1080/17452759.2014.900857.

[8] M. Cabrini, A. Carrozza, S. Lorenzi, T. Pastore, C. Testa, D. Manfredi, P. Fino, F. Scenini, Influence of surface finishing and heat treatments on the corrosion resistance of LPBF-produced Ti-6Al-4V alloy for biomedical applications, J. Mater. Process Technol. 308 (2022), https://doi.org/10.1016/j.jmatprotec.2022.117730.

[9] S. Nikpour, J.D. Henderson, S. Matin, H.Y. Nie, J. Hedberg, V. Dehnavi, Y. K. Hosein, D.W. Holdsworth, M. Biesinger, Y.S. Hedberg, Effect of passivation and surface treatment of a laser powder bed fusion biomedical titanium alloy on corrosion resistance and protein adsorption, Electro Acta 475 (2024), https://doi.org/10.1016/j.electacta.2023.143650.

[10] L.Y. Chen, H.Y. Zhang, C. Zheng, H.Y. Yang, P. Qin, C. Zhao, S. Lu, S.X. Liang, L. Chai, L.C. Zhang, Corrosion behavior and characteristics of passive films of laser powder bed fusion produced Ti–6Al–4V in dynamic Hank's solution, Mater. Des. 208 (2021), https://doi.org/10.1016/j.matdes.2021.109907.

[11] D. Fischer, K. yuan Cheng, M.Q. Neto, D. Hall, D. Bijukumar, A.A. Espinoza Orías, R. Pourzal, R.J. van Arkel, M.T. Mathew, Corrosion behavior of selective laser melting (SLM) manufactured Ti6Al4V alloy in saline and BCS solution, J. Bio Tribocorros 8 (2022), https://doi.org/10.1007/s40735-022-00657-1.

[12] A. Bordbar-Khiabani, M. Gasik, Electrochemical and biological characterization of Ti–Nb–Zr–Si alloy for orthopedic applications, Sci. Rep. 13 (2023), https://doi.org/10.1038/s41598-023-29553-5.

[13] J.P. Bearinger, C.A. Orme, J.L. Gilbert, Effect of hydrogen peroxide on titanium surfaces: In situ imaging and step-polarization impedance spectroscopy of commercially pure titanium and titanium, 6-aluminum, 4-vanadium, J. Biomed. Mater. Res A 67 (2003) 702–712, https://doi.org/10.1002/jbm.a.10116.

[14] M.A. Kurtz, A.C. Wessinger, L.M. Taylor, J.L. Gilbert, Electrode potential, inflammatory solution chemistry and temperature alter Ti-6Al-4V oxide film properties, Electro Acta 462 (2023), https://doi.org/10.1016/j.electacta.2023.142770.

[15] A. Sotniczuk, W. Chromiński, B. Adamczyk-Cieślak, M. Pisarek, H. Garbacz, Corrosion behaviour of biomedical Ti under simulated inflammation: Exploring the

relevance of grain refinement and crystallographic texture, Corros. Sci. 200 (2022), https://doi.org/10.1016/j.corsci.2022.110238.
[16] A. Sotniczuk, J.L. Gilbert, Y. Liu, M. Matczuk, W. Chromiński, D. Kalita, M. Pisarek, H. Garbacz, Corrosion resistance of β-phase titanium alloys under simulated inflammatory conditions: exploring the relevance of biocompatible alloying elements, Corros. Sci. 220 (2023), https://doi.org/10.1016/j.corsci.2023.111271.
[17] F. Yu, O. Addison, A.J. Davenport, A synergistic effect of albumin and H2O2 accelerates corrosion of Ti6Al4V, Acta Biomater. 26 (2015) 355–365, https://doi.org/10.1016/j.actbio.2015.07.046.
[18] J.Y. Cho, W. Xu, M. Brandt, M. Qian, Selective laser melting-fabricated Ti-6Al-4V alloy: microstructural inhomogeneity, consequent variations in elastic modulus and implications, Opt. Laser Technol. 111 (2019) 664–670, https://doi.org/10.1016/j.optlastec.2018.08.052.
[19] G. Buffa, D. Palmeri, G. Pollara, F. Di Franco, M. Santamaria, L. Fratini, Process parameters and surface treatment effects on the mechanical and corrosion resistance properties of Ti6Al4V components produced by laser powder bed fusion, Prog. Addit. Manuf. 9 (2024) 151–167, https://doi.org/10.1007/s40964-023-00440-9.
[20] H. Ishizawa, M. Ogino, J. Wiley, Formation and characterization of anodic titanium oxide films containing Ca and P, n.d.
[21] H. Ishizawa, M. Fujino, M. Ogino, Mechanical and histological investigation of hydrothermally treated and untreated anodic titanium oxide films containing Ca and P, n.d.
[22] H. Ishizawa, M. Ogino, Characterization of thin hydroxyapatite layers formed on anodic titanium oxide films containing Ca and P by hydrothermal treatment, n.d.
[23] B. Hirschorn, M.E. Orazem, B. Tribollet, V. Vivier, I. Frateur, M. Musiani, Determination of effective capacitance and film thickness from constant-phase-element parameters, Electro Acta 55 (2010) 6218–6227, https://doi.org/10.1016/j.electacta.2009.10.065.
[24] 1998, N. Sato, Electrochemistry at Metal and Semiconductor Electrodes, 1998..
[25] F. Di Franco, A. Zaffora, D. Pupillo, L. Iannucci, S. Grassini, M. Santamaria, The effect of electronic properties of anodized and hard anodized Ti and Ti6Al4V on their reactivity in simulated body fluid, J. Electrochem Soc. 169 (2022) 071506, https://doi.org/10.1149/1945-7111/ac8316.
[26] C. Fonseca, M.A. Barbosa, Corrosion behaviour of titanium in biofluids containing H 2 O 2 studied by electrochemical impedance spectroscopy, n.d. ⟨www.elsevier.com/locate/corsciCorrosionScience43⟩.
[27] M.B. Leban, T. Kosec, M. Finšgar, Corrosion characterization and ion release in SLM-manufactured and wrought Ti6Al4V alloy in an oral environment, Corros. Sci. 209 (2022), https://doi.org/10.1016/j.corsci.2022.110716.